ACS APPLIED MATERIALS & INTERFACES

Research Article

www.acsami.org

Iridium Oxide Nanoparticles and Iridium/Iridium Oxide Nanocomposites: Photochemical Fabrication and Application in Catalytic Reduction of 4-Nitrophenol

Di Xu,[†] Peng Diao,*[,†] Tao Jin,[†] Qingyong Wu,[†] Xiaofang Liu,[†] Xin Guo,[†] Hongyu Gong,[‡] Fan Li,[‡] Min Xiang,[†] and Yu Ronghai[†]

[†]School of Materials Science and Engineering, Beihang University, Xueyuan Road No. 37, Haidian District, Beijing 100191, PR China

[‡]College of Environmental and Energy Engineering, Beijing University of Technology, Beijing 100124, PR China

Supporting Information

ABSTRACT: Hydrous iridium oxide (IrO_x) nanoparticles (NPs) with an average diameter of 1.7 ± 0.3 nm were prepared via photochemical hydrolysis of iridium chloride in alkaline medium at room temperature. The photoinduced hydrolysis was monitored by time-dependent ultraviolet−visible (UV−vis) spectroscopy, and the effects of the incident wavelength and irradiation time on the production of IrO_x NPs were systematically investigated. It was found that UV−vis irradiation is crucial for the generation of IrO_x NPs during the hydrolysis of $IrCl_3$, and once the irradiation was turned off, the hydrolysis reaction stopped immediately. The production rate of IrO_x NPs greatly depended on the incident wavelength. There is a critical wavelength of 500 nm for the hydrolysis reaction, and IrO_x NPs can only be produced under the illumination with an incident wavelength shorter than 500 nm. Moreover, the shorter the incident wavelength, the faster the growth rate of IrO_x NPs. The obtained IrO_x NPs were highly stable during two months of storage at 4 °C. The Ir/IrO_x nanocomposites were prepared by surface reduction of IrO_x NPs with $NaBH_4$. The microstructure of the Ir/IrO_x composite was characterized by transmission electron microscopy (TEM), and the presence of zero-valence Ir was confirmed by the X-ray diffraction (XRD) result. The Ir/IrO_x nanocomposite exhibited good catalytic activity and high recycling stability toward the reduction of 4-nitrophenol. The catalytic activity per unit surface area of the Ir/IrO_x composite catalyst was increased by a factor of 15 compared to that of pure Ir catalyst. The presence of the Ir/IrO_x interfaces in the composite catalyst is believed to be responsible for the high activity.

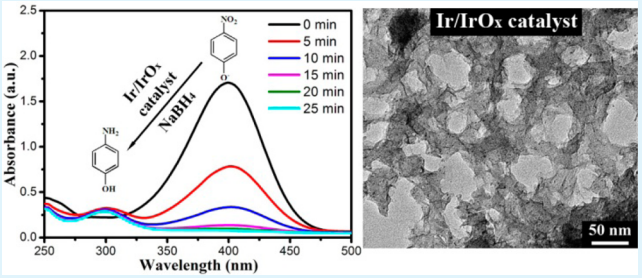

KEYWORDS: *photochemistry, iridium oxide, nanocomposite, catalysis, 4-nitrophenol*

1. INTRODUCTION

Over the past few decades, noble metals and their oxides have attracted extensive attention because of their promising application in various fields including detecting and sensing,[1] fuel cells,[2] and catalysis.[3,4] However, their low terrestrial abundance results in the high cost of noble metals and their oxides, which has greatly restricted their large-scale applications in industry. Synthesizing particles with high mass activity (activity per unit mass) provides an alternative solution. There are mainly two strategies to improve the mass activity of the particles: first, to enlarge the specific surface area of the particle by simply decreasing the particle size, and second, to create more active sites on the particles. The latter strategy is usually accomplished by exposing highly active crystalline facets[5] or creating active interfaces by constructing binary structures.[6] To develop a highly active noble metal catalyst, it is desirable to combine the above two strategies together, that is, to prepare metals and their oxide NPs with precise control of their composition, size, and morphology. Great efforts have been made on size- and morphology-controlled synthesis of noble metals and their oxide NPs, including Ag,[7] Au,[8] Pd,[9] Pt,[10] Rh,[11] Ir,[12] and IrO_2.[13]

To control the composition, size, and morphology of metal or metal oxide NPs, it is essential to understand their formation mechanism. The feasibility and convenience of stopping the reaction at any desired time and taking samples for characterization and analysis is very important for the exploration of the formation mechanism. Photochemical synthesis is a convenient way to carry out the investigation of NPs growth because of the following two reasons: (1) Light irradiation can provide a driving force for the reduction or oxidation of the precursors, thereby promoting the generation of metal and metal oxide NPs.[14,15] (2) The photoinduced synthesizing reactions can be easily initiated or terminated at any time by simply turning on or off the irradiation. Therefore, the photochemical method is an important tool for the study of the generation and growth of

Received: May 24, 2015
Accepted: July 9, 2015
Published: July 9, 2015

ACS Publications © 2015 American Chemical Society

DOI: 10.1021/acsami.5b04504
ACS Appl. Mater. Interfaces 2015, 7, 16738−16749

NPs.[16] Moreover, it is possible to modulate the growth rate, size, morphology, and orientation of the NPs by carefully tuning the irradiation parameters, such as incident wavelength,[17] power density,[18] and polarization of the light.[19] Thus, photochemical routes have been widely employed in the synthesis of metal and metal oxide NPs. Numerous works have been focused on the light-assisted preparation of noble metal NPs, including Ag,[20] Au,[21] Pd,[22] and Pt.[23] However, the photochemical synthesis of iridium and iridium oxide (IrO_x) NPs was rarely reported.[24,25] Usually, IrO_x NPs were prepared by thermal hydrolysis of Ir(IV) or Ir(III) precursors;[26,27] for example, the Mallouk group produced IrO_x NPs with a size of less than 2 nm via the hydrolysis of Ir(IV) precursor ($[IrCl_6]^{2-}$) in basic medium.[26] The hydrolysis of iridium precursor is very slow at room temperature; thus, additional energy is usually required to accelerate the reaction. Therefore, the reaction temperature was usually raised to 70−90 °C to drive the hydrolysis to completion.[26] In this work, light was used instead of heat to provide energy to drive the hydrolysis of $IrCl_3$ at room temperature.

Previous work has revealed that when the metal NPs are grown on metal oxide substrates their catalytic activity can be significantly improved.[28−30] For example, Ag/TiO_2,[31] Pt/Fe_2O_3,[32] and Ni/TiO_2[33] composites exhibit catalytic activity superior to that of pure metal or metal oxide catalysts. Among these hybrid catalysts, M/MO_x composites (M stands for one metal element) are especially interesting, not only because of their high catalytic activity but also because of their ease preparation. The M/MO_x composites can be fabricated simply by first synthesizing metal (or metal oxide) particles and then partially oxidizing (or reducing) their surfaces. Successful preparation of catalytically active M/MO_x systems, such as Ru/RuO_2,[34] Pd/PdO,[35] and Au/Au_2O_3,[36] have been reported in previous works, proving that the interface between metal and metal oxide is beneficial for improving the catalytic activity of pristine metal catalysts. However, little attention is paid to the Ir/IrO_x system. Because both Ir and IrO_x are present at the Ir/IrO_x interface, the synergic effect of Ir and IrO_x may benefit the catalytic activity of the Ir/IrO_x composite. In this work, we aim to generate the Ir/IrO_x interface by preparation of the Ir/IrO_x nanocomposite and evaluating its catalytic activity toward the reduction of 4-nitrophenol.

4-Nitrophenol is a toxic organic pollutant in industrial wastes, and it is highly stable in biological systems. Thus, it may threaten the health of humans and animals. As a result, it is necessary to develop effective ways for the degradation of 4-nitrophenol. In principle, 4-nitrophenol can be removed via either an oxidative or a reductive route. The goal of oxidative degradation is to totally oxidize 4-nitrophenol to CO_2, NO_3^-, and H_2O. However, the oxidation of 4-nitrophenol usually involves a series of reactions including ring opening,[37] and the complexity of the reactions makes it difficult to fulfill total decomposition of 4-nitrophenol. The reductive route is aimed at converting 4-nitrophenol into 4-aminophenol, and the latter is an important intermediate in the manufacture of dyes,[38] photographic developers,[39] and antipyretic drugs.[40] Although reductive degradation may not be the final solution, the produced 4-aminophenol is less toxic than 4-nitrophenol,[41] and it can be further degraded by microorganisms.[42] Therefore, the conversion of 4-nitrophenol to 4-aminophenol has attracted extensive attention. The reduction of 4-nitrophenol is typically operated at high temperature and hydrogen pressure;[43] thus, the route for reducing 4-nitrophenol under relatively mild conditions is highly desirable. The reduction of 4-nitrophenol by $NaBH_4$ at room temperature is a possible solution, and this model reaction has been widely investigated using noble-metal-based catalysts including Ag,[44] Au,[45] and Pt−Ni.[46] However, no work was reported on the reduction of 4-nitrophenol on Ir-based catalysts that are well-known for their catalytic activity toward organic dye degradation,[24] hydrogenation,[47] and oxygen reduction[48] reactions.

In this work, we report the preparation of IrO_x NPs via a photopowered hydrolysis method, in which illumination was used to initiate and accelerate the hydrolysis of iridium precursor. We find that only when the incident wavelength is shorter than a threshold wavelength of 500 nm can the hydrolysis reaction occur. We demonstrate that the Ir/IrO_x nanocomposite can be obtained by partially reducing IrO_x to metal Ir on the surface of IrO_x NPs. We also demonstrate that the Ir/IrO_x nanocomposite is a promising catalyst for the reduction of 4-nitrophenol.

2. EXPERIMENTAL SECTION

2.1. Materials. Iridium chloride trihydrate ($IrCl_3 \cdot 3H_2O$) was purchased from Alfa Aesar company. Sodium borohydride ($NaBH_4$) was obtained from Tianjin Fuchen Chemical Reagents Factory. Potassium hydroxide (KOH), sodium hydroxide (NaOH), nitric acid (HNO_3, 65−68 wt %), and absolute ethanol were purchased from Beijing Chemical Reagents Corporation. 4-Nitrophenol and 4-aminophenol were obtained from Sinopharm Chemical Reagent Corporation, Ltd. All other chemicals were of analytical grade and used without further purification. All aqueous solutions were prepared with ultrapure water (18 MΩ cm).

2.2. Photochemical Synthesis of IrO_x NPs. Iridium oxide NPs were prepared via a photochemical hydrolysis approach. In a typical procedure, an aqueous solution of 2 mM $IrCl_3$ was prepared in a beaker, and the pH of solution was adjusted to 12 with concentrated KOH. Then, the beaker was placed under polychromatic or monochromatic light irradiation. During photochemical synthesis, the reaction system was kept at room temperature by a circulating water bath. The UV light was generated from a PLS-SXE300UV xenon lamp equipped with a UV reflection filter (Beijing Perfect Light Science and Technology Co., Ltd., output wavelength: 260−410 nm) and different bandpass filters to furnish monochromatic light with the wavelengths required. The power densities of both UV and monochromatic light irradiation on the solution were 5 mW/cm^2. During irradiation, the color of the solution changed from clear yellow to dark blue, implying the generation of IrO_x NPs.[26] To monitor the reaction, samples of the solution were taken out at fixed time intervals and diluted for the UV−vis characterization. After photochemical reaction, the obtained colloid solution was stored in a refrigerator at 4 °C.

2.3. Preparation of the Ir, IrO_x, and Ir/IrO_x Composite Catalysts. Three kinds of catalysts were prepared in this work, and they were denoted as IrO_x, Ir, and Ir/IrO_x, respectively. The IrO_x catalyst was obtained through acidic condensation by adding HNO_3 to the as-prepared IrO_x colloid solution. The precipitate formed was rinsed with water until a pH value of 7 was attained and then redispersed in water. In the preparation of Ir catalyst, 5 mL of 2 mM $IrCl_3$ solution with a pH value of 12 was mixed with 5 mL of 0.2 M $NaBH_4$, and the mixture was transferred to a three-necked flask connected to a reflux system. The reaction system was heated in an oil bath at 90 °C under stirring for 30 min. The product was separated by repeated centrifugation at 12 000 rpm and then rinsed with copious water. Then, the final precipitate was also redispersed in water. The approach to synthesizing Ir/IrO_x catalyst is quite similar to the one used to synthesize Ir catalyst. The only difference is that 5 mL of IrO_x NP colloid solution was used instead of 2 mM $IrCl_3$ solution. After partial reduction by $NaBH_4$, the resulting Ir/IrO_x catalyst was rinsed with copious water and redispersed in water. The iridium

DOI: 10.1021/acsami.5b04504
ACS Appl. Mater. Interfaces 2015, 7, 16738−16749

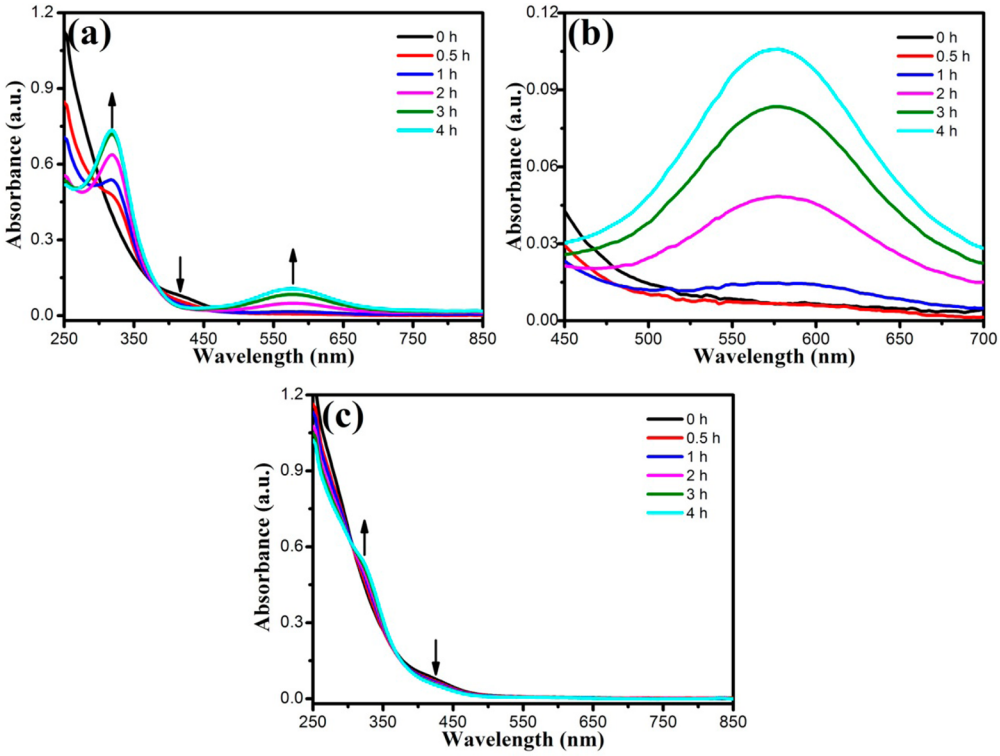

Figure 1. Time-dependent UV−vis spectra of 2 mM $IrCl_3$ solutions at pH 12 (a and b) under UV irradiation and (c) in the dark. Panel b is the magnified spectra of a in the wavelength range of 450−700 nm. UV irradiation was supplied by a polychromatic light source with output wavelength of 260−410 nm.

concentrations (including all valence states) in the colloid solutions of the above three catalysts were identical to each other.

2.4. Characterization. The UV−vis absorption spectra were recorded using a UV2600 spectrophotometer (Tianmei Co., China). The Ir, IrO_x, and Ir/IrO_x catalysts were characterized by transmission electron microscopy (TEM, JEM-2100F, JEOL, Japan, accelerating voltage: 200 kV) and X-ray diffraction (XRD, Rigaku X-ray diffractometer, Japan, Cu Kα source, 40 kV, 40 mA). For the TEM characterization, the catalysts were dispersed in ethanol, and the resulting solution was then dropped onto the copper-grid-supported carbon film to prepare the TEM samples. The specific surface areas of Ir/IrO_x and Ir catalysts were determined by Brunauer−Emmett−Teller method (BET, Autosorb iQ, Quantachrome Instruments, USA) with nitrogen as adsorption gas. The catalyst powder was placed in a test tube and degassed for 6 h at 300 °C under vacuum ($p < 10^{-4}$ Pa). The N_2 adsorption−desorption isotherms were obtained as a function of relative pressure (p/p_0 = 0.024−0.994, where p and p_0 are the equilibrium vapor pressure and the saturation vapor pressure of N_2 at 77.35 K, respectively). The specific surface areas of the catalysts were calculated on the basis of BET interpretation of the adsorption curves at p/p_0 = 0.1−0.25. A cross-sectional area of 0.162 nm^2 was assumed for the N_2 molecule. X-ray photoelectron spectroscopic (XPS) measurements were carried out on a PHI Quantera SXM scanning X-ray microprobe (ULVAC-PHI, Japan), with a monochromatic Al source at a power of 25 W. The measurement was carried out under a pressure of 4.5×10^{-7} Pa. The binding energies were calibrated to the C 1s line at 284.8 eV, and Shirley background subtraction was applied to the raw data before deconvolution.

2.5. Catalytic Reduction of 4-Nitrophenol Using Ir, IrO_x, and Ir/IrO_x as Catalysts. The activity of the Ir, IrO_x, and Ir/IrO_x catalysts were evaluated via the catalytic reduction of 4-nitrophenol by $NaBH_4$, and the reaction was carried out in a quartz cuvette at room temperature. The colloid solution of as-prepared catalyst (40 μL, 2 mM on the basis of Ir concentration including all valence states) and 10 μL of 4-nitrophenol stock solution (20 mM) were mixed in 3.8 mL of water. Then, 200 μL of 0.2 M $NaBH_4$ solution that was freshly prepared in ice bath was quickly injected into the mixed solution. The final concentrations of catalyst, 4-nitrophenol, and $NaBH_4$ in the reaction solution were 20 μM, 50 μM, and 10 mM, respectively. Then, UV−vis spectra of the reaction solutions were recorded at fixed time intervals. The leaching of iridium into the solution during the consecutive catalytic cycles was quantified by inductively coupled plasma-atomic emission spectroscopy on an Optima 7000 DV spectrometer (PerkinElmer, USA).

3. RESULTS AND DISCUSSION

3.1. Photoinduced Production of IrO_x NPs. UV irradiation was introduced to accelerate the hydrolysis of $IrCl_3$ solution at pH 12 at room temperature. Time-dependent UV−vis spectroscopy was employed to monitor the reaction process, and the results are presented in Figure 1. The $IrCl_3$ solution at pH 12 shows a weak hump around 400 nm (Figure 1a) that was assigned to $Ir(H_2O)_3Cl_3$,[49] the product of aquation of $IrCl_3$ in aqueous solution.[50] After 0.5 h of UV irradiation, a shoulder peak at ca. 320 nm arises, whereas the hump at 400 nm decreases. According to the previous reports,[27,51] the 320 nm peak originates from $[Ir(OH)_6]^{3-}$. With continuous UV irradiation, the 320 nm peak becomes sharper and more intense and reaches its maximum after 3 h, whereas the hump at 400 nm keeps decreasing. These phenomena indicate that $Ir(H_2O)_3Cl_3$ is continuously converted to iridium hydroxide complex $[Ir(OH)_6]^{3-}$ during illumination. The reaction can be expressed by the following equation:

$$Ir(H_2O)_3Cl_3 + 6OH^- \rightarrow [Ir(OH)_6]^{3-} + 3Cl^- + 3H_2O \quad (1)$$

The presence of the isosbestic point at ca. 380 nm in Figure 1a implies that the reaction proceeded without producing byproducts.

DOI: 10.1021/acsami.5b04504
ACS Appl. Mater. Interfaces 2015, 7, 16738−16749

With the conversion of $Ir(H_2O)_3Cl_3$ to $[Ir(OH)_6]^{3-}$, a broad absorption band centered at 580 nm appears and keeps growing with elongated irradiation time. This observation implies the generation of iridium oxide NPs, which have a characteristic absorption band around 580 nm.[26] As is indicated by the magnified spectra shown in Figure 1b, IrO_x NP were not produced immediately after 0.5 h of UV irradiation when $[Ir(OH)_6]^{3-}$ had been generated. Instead, IrO_x NPs appeared after 1 h of irradiation. The significant 0.5 h delay between the appearance of the 580 nm peak and that of the 320 nm shoulder peak implies that the accumulation of $[Ir(OH)_6]^{3-}$ is a prerequisite for the generation of IrO_x NPs. Therefore, it can be inferred that when the concentration of $[Ir(OH)_6]^{3-}$ is sufficiently high $[Ir(OH)_6]^{3-}$ polymerizes to generate Ir_2O_3 and part of Ir_2O_3 can be further oxidized to IrO_2 by dissolved oxygen:

$$2[Ir(OH)_6]^{3-} \rightarrow Ir_2O_3 + 3H_2O + 6OH^- \quad (2)$$

$$2Ir_2O_3 + O_2 \rightarrow 4IrO_2 \quad (3)$$

Because of the coexistence of Ir(III) and Ir(IV), the obtained NPs are denoted as IrO_x NPs. To confirm the effect of UV irradiation, the hydrolysis of $IrCl_3$ was also carried out in the dark, and the result is shown in Figure 1c. The peak at 580 nm, which corresponds to IrO_x NPs, does not appear even after 4 h, implying that no IrO_x NPs were formed. This observation clearly indicates that UV irradiation has greatly promoted the hydrolysis of $IrCl_3$ and the generation of IrO_x NPs.

On the basis of the thermal hydrolysis mechanism of iridium precursor,[26] we believe that the photoinduced generation of IrO_x NPs involves the following two successive steps: (1) UV illumination induces the fast hydrolysis of $IrCl_3$ in alkaline medium to form $[Ir(OH)_6]^{3-}$. (2) The $[Ir(OH)_6]^{3-}$ complex ions polymerize to produce IrO_x NPs when the concentration of $[Ir(OH)_6]^{3-}$ is sufficiently high. The increasing of 320 and 580 nm peaks corresponds to steps 1 and 2, respectively. It should be pointed out here that even after IrO_x NPs is produced the 320 nm peak still keeps increasing until the total irradiation time reaches 4 h. This is probably because step 1 is faster than step 2, and the particle generation reaction finally approaches equilibrium after 4 h of illumination.

The stability of the obtained colloid solutions of IrO_x NPs is very high, as can be seen from the fact that their UV−vis spectra experienced negligible change even after two months of aging at 4 °C (Figure S1 in the Supporting Information). Moreover, no precipitates were observed after aging for several months at room temperature. According to the literature,[52] the IrO_x NPs were negatively charged in basic solution because of the adsorption of large amount of OH^- on their surface, and the electrostatic repelling prevented the IrO_x NPs from aggregating, resulting in the high stability of the colloid solution.

3.2. Effect of UV Irradiation Time on the Production of IrO_x NPs. UV irradiation has been proven to play a promoting role in the generation of IrO_x NPs. However, whether it affects the overall reaction process or just triggers the reaction in the initial stage remains unclear. To further elucidate the effect of UV irradiation, time-dependent UV−vis spectra of the reaction solution were recorded at different irradiation times. Figure 2 shows the peak absorbance of IrO_x NPs at 580 nm as a function of irradiation time. (See Figure S2 in the Supporting Information for change of UV−vis spectra.) When the UV irradiation is turned off, the increase of the peak absorbance slows down immediately. This phenomenon provides direct evidence that the key effect of UV irradiation on the generation of IrO_x NPs exists during the whole reaction process. It can be safely concluded that UV irradiation offers the driving force for the hydrolysis of $IrCl_3$ and the formation of IrO_x NPs, rather than simply triggering the reaction in the initial stage. Therefore, one can control the reaction by varying the irradiation time.

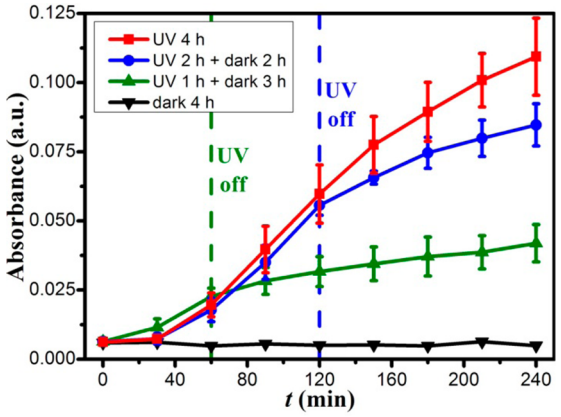

Figure 2. Absorbance profiles at 580 nm as a function of time for 2 mM $IrCl_3$ solutions at pH 12 under different illumination conditions: continuous UV irradiation for 4 h (red), UV irradiation for 2 h followed by 2 h in the dark (blue), UV irradiation for 1 h followed by 3 h in the dark (green), and kept in dark for 4 h (black).

3.3. Effect of Irradiation Wavelength on the Production of IrO_x NPs. Previous works have confirmed that in the photochemical synthesis of noble metal NPs the incident wavelength is an important factor affecting the growth process of the products.[17] By selecting different incident wavelengths, the growth rate of the NPs can be precisely controlled. Generally, longer wavelengths result in slower growth of NPs.[17] In this work, to examine the effect of incident wavelength on the growth of IrO_x NPs, monochromatic light was also employed to promote the hydrolysis of $IrCl_3$.

Figure 3 shows the time-dependent UV−vis spectra of $IrCl_3$ solution under monochromatic illumination of different wavelengths at the same power density of 5 mW/cm^2. The IrO_x NPs were produced after 4 h of monochromatic illumination, as can be seen from the presence of the absorption peak of IrO_x NPs at 580 nm (Figure 3a−c).[26] This observation proves that besides polychromatic light monochromatic light can also power the production of IrO_x NPs. If the wavelength is increased to 500 nm, however, then IrO_x NPs can no longer be obtained after 4 h of irradiation, as is shown in Figure 3d. These results imply that there exists an upper limit of the incident wavelength (500 nm) for promoting the reaction.

Because the peak absorption intensity at 580 nm reflects the concentration of IrO_x NPs in colloid solution, it was used to monitor the particles generation rate, and the results are shown in Figure 4. The slope of the curve implies the production rate of IrO_x NPs: the larger the slope, the fast the production rate. It is seen from Figure 4 that the generation rate of IrO_x NPs under different monochromatic light follows the order 350 nm >380 nm >420 nm >500 nm. These results confirm that a shorter incident wavelength results in faster reaction kinetics for the generation of IrO_x NPs. We believe this is because the light with shorter wavelength has higher photon energy and provides

DOI: 10.1021/acsami.5b04504
ACS Appl. Mater. Interfaces 2015, 7, 16738−16749

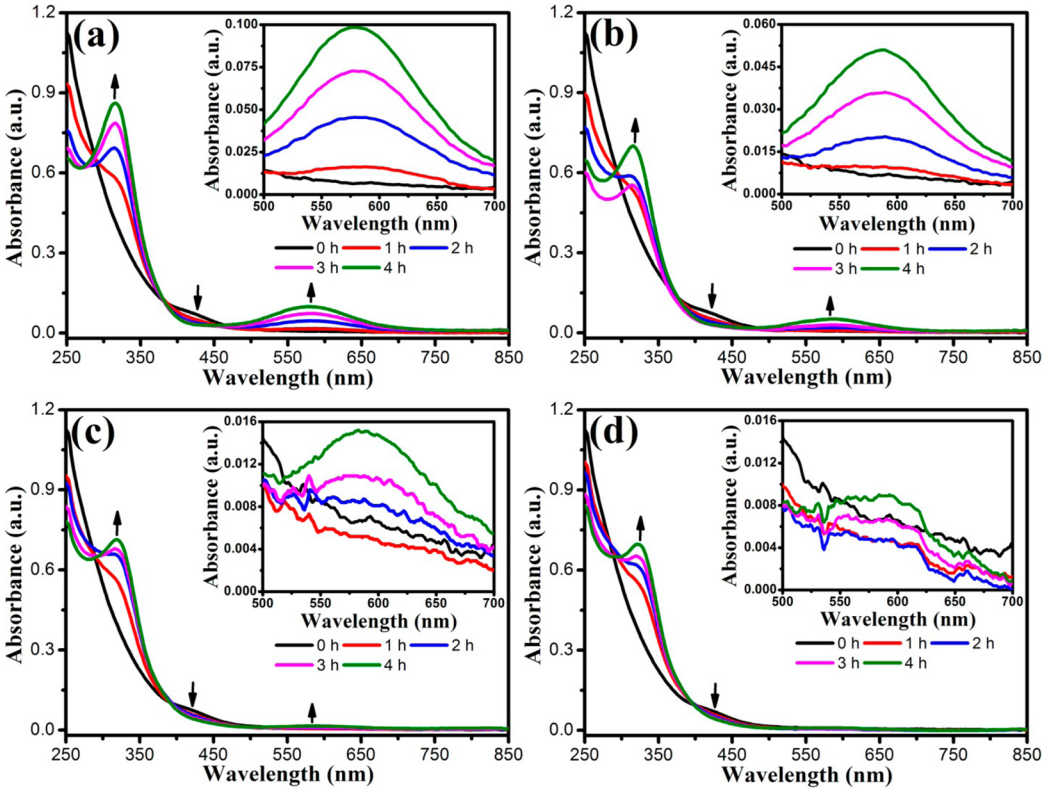

Figure 3. Time-dependent UV−vis spectra of 2 mM $IrCl_3$ solutions at pH 12 under (a) 350 nm, (b) 380 nm, (c) 420 nm, and (d) 500 nm monochromatic light irradiation. The power density of irradiation was 5 mW/cm^2. The insets are the magnified absorption bands from 500 to 700 nm.

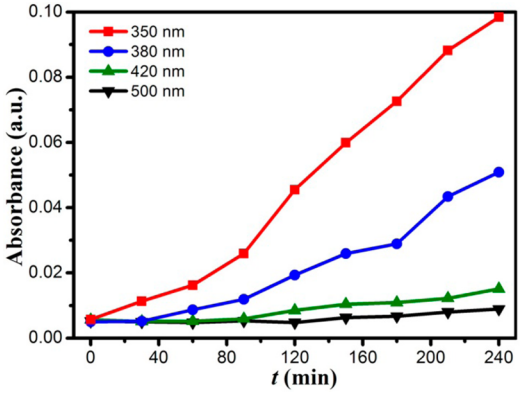

Figure 4. Absorbance profiles of 2 mM $IrCl_3$ solution (pH 12) at 580 nm as a function of time during photoinduced generation of IrO_x NPs under monochromatic illumination by different wavelengths.

a larger driving force for the photopowered generation of IrO_x NPs.

3.4. Characterization of IrO_x, Ir, and Ir/IrO_x Catalysts.

The morphology and the particle size of the IrO_x NPs were characterized by TEM, and the results are presented in Figure 5. A typical TEM image (Figure 5a) demonstrates that the IrO_x NPs are uniformly dispersed without obvious aggregation. The small aggregates observed in the TEM image were formed during the evaporation of the solvent when preparing the TEM sample. The HRTEM image indicates that the IrO_x NPs are irregularly shaped (Figure 5b). The lattice spacing of IrO_x NPs does not match well with either IrO_2 or Ir_2O_3, and it even changes within one particle, implying an amorphous structure with both Ir(III) and Ir(IV) coexisting in IrO_x NPs.[53] The average diameter of the IrO_x NPs is 1.7 ± 0.3 nm (Figure 5c), which is obtained from statistic data of over 200 individual NPs. This is in good accordance with the results reported in the literature,[3,26] in which the IrO_x NPs were prepared through thermal hydrolysis of iridium precursor. The small size of the IrO_x NPs indicates that the growth of IrO_x NPs is greatly inhibited by the adsorbed OH^- because OH^- is found to retard the growth of metal oxide NPs via surface adsorption.[54]

The IrO_x NP powder was obtained from the colloid solution via acidic precipitation. As is mentioned above, the IrO_x NPs are negatively charged because of the adsorption of OH^-. Upon the introduction of acid into the colloid solution, the adsorbed OH^- will be neutralized by H^+; thus, the electrostatic repelling between IrO_x NPs no long exists, leading to the aggregation of particles.[52] Figure 6a shows a typical TEM image of the IrO_x NP precipitates, from which it can be seen that the precipitates have a network structure. The HRTEM image (Figure 6b) reveals that the network structure is composed of NPs with an average diameter of ca. 2 nm, suggesting that the small IrO_x NPs do not merge into large particles during precipitation. This ensures that the IrO_x NPs have a large specific area, which is very important when they are used as a catalyst.

The Ir NPs and the Ir/IrO_x composite NPs were also prepared and employed as a catalyst for 4-nitrophenol reduction. As shown in Figure 6c, the Ir NPs, which were prepared by reducing $IrCl_3$ with $NaBH_4$ at 90 °C, are composed of nanoparticles with particle size in the range of 2−5 nm. Figure 6d shows a typical HRTEM image of Ir catalyst. The lattice fringe spacing of Ir NPs is 0.220 nm, which corresponds to the facets of face-centered cubic (fcc) iridium.[55] The Ir/IrO_x composite NPs were synthesized via reducing the surface Ir(III)

DOI: 10.1021/acsami.5b04504
ACS Appl. Mater. Interfaces 2015, 7, 16738−16749

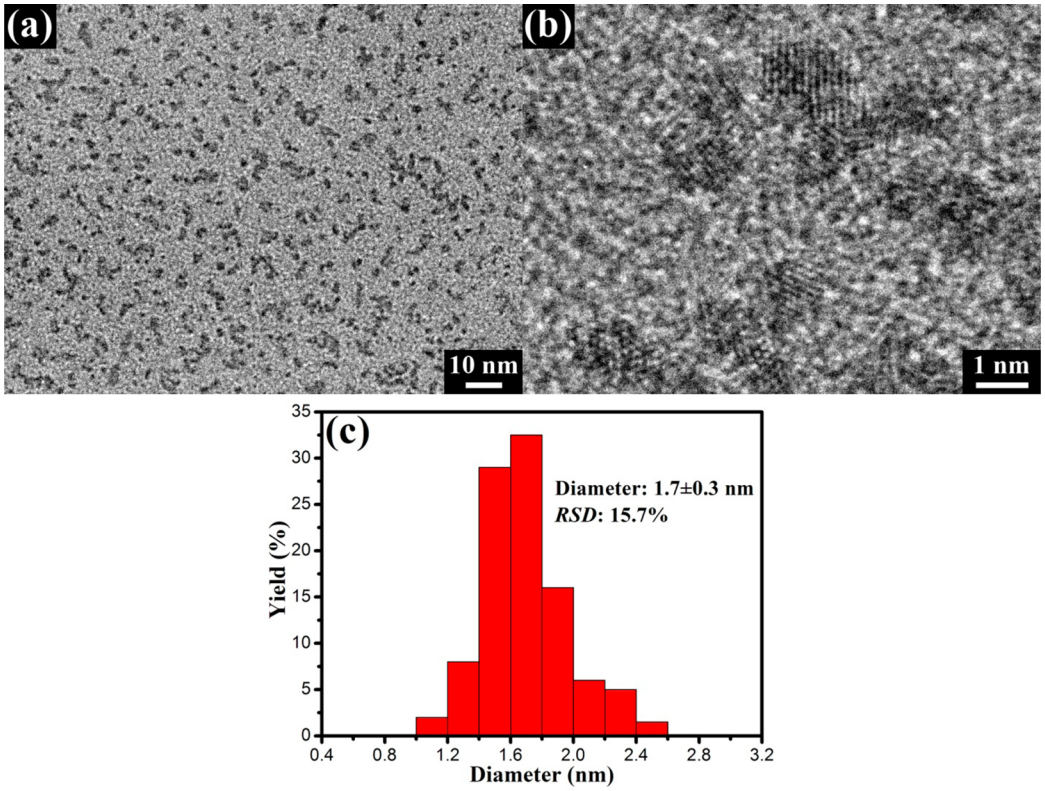

Figure 5. Typical (a) TEM and (b) HRTEM images of IrO_x NPs. (c) Size distribution histogram of IrO_x NPs, in which RSD stands for relative standard deviation.

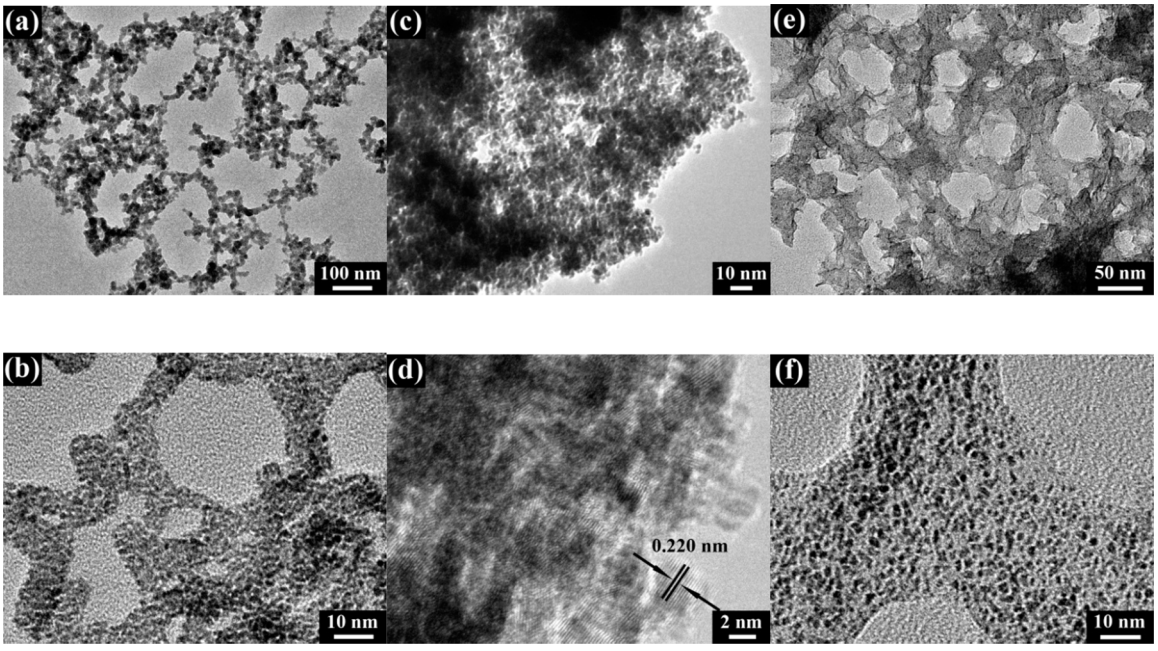

Figure 6. Typical TEM images of (a and b) IrO_x, (c and d) Ir, and (e and f) Ir/IrO_x catalysts under low (a, c, and e) and high (b, d, and f) magnification.

(or Ir(IV)) to zero-valent iridium on IrO_x NPs by $NaBH_4$ at 90 °C. TEM image (Figure 6e) indicates that the Ir/IrO_x composite NPs have a sheet structure, and the HRTEM image shown in Figure 6f reveals that the sheet structure is composed of small Ir/IrO_x NPs. The reason for the formation of the sheet structure is not currently clear.

The crystalline properties of the IrO_x, Ir, and Ir/IrO_x composite catalysts were also characterized by XRD, and the result is shown in Figure 7. The IrO_x catalyst exhibits only two broad bumps in XRD spectrum, indicating its amorphous nature. The XRD pattern of Ir catalyst shows two broadened diffraction peaks that are in good agreement with the standard pattern of fcc iridium (Powder Diffraction File no. 06-598,

DOI: 10.1021/acsami.5b04504
ACS Appl. Mater. Interfaces 2015, 7, 16738−16749

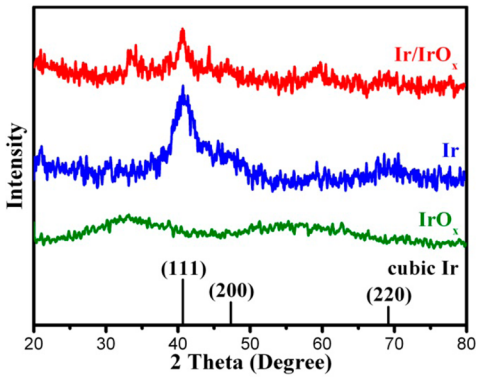

Figure 7. XRD patterns of the IrO_x, Ir, and Ir/IrO_x catalysts.

International Centre for Diffraction Data, 2002), confirming that the Ir catalyst consists of zero-valent iridium. The size of Ir NPs can be estimated by the Debye–Scherrer formula:[56]

$$D = 0.9\lambda/\beta \cos\theta \quad (4)$$

where the D is the average size of the Ir NPs, λ is the wavelength of incident X-ray (in this work, λ = 0.15406 nm), and β and θ are the full width at half-maximum and position of the diffraction peak, respectively. The average size of the Ir NPs is ca. 3.7 nm using the (111) peak (40.66°) for calculation. This value is in good agreement with the one estimated from the TEM images. The diffraction peaks of zero-valent Ir can also be detected on Ir/IrO_x catalyst, confirming that Ir/IrO_x composite was successfully prepared by surface reduction of IrO_x NPs with $NaBH_4$ at 90 °C. Here, it should be pointed out that no diffraction peaks of the metal Ir were obtained (data not shown) when the reduction was carried out at room temperature. This observation implies that the Ir/IrO_x composite cannot be produced by reducing surface IrO_x to Ir at room temperature.

3.5. Catalytic Activity of IrO_x, Ir and Ir/IrO_x Catalysts toward 4-Nitrophenol Reduction. Herein, the IrO_x, Ir, and Ir/IrO_x composite were employed as catalysts to reduce 4-nitrophenol. As shown in Figure 8a, the 4-nitrophenol solution (pH 5) shows an absorption peak at 317 nm. However, after $NaBH_4$ is injected into the solution, the absorption peak shifts immediately to 400 nm. This is due to the fact that the addition of $NaBH_4$ increases the pH of the mixed solution (pH 8), which results in the ionization of 4-nitrophenol to 4-nitrophenolate, and the latter has a characteristic absorption peak at 400 nm.[57] This result can be further confirmed by the UV–vis spectra of the 4-nitrophenol solution whose pH was adjusted to 7 by adding NaOH. (See the solid line in Figure 8a.)

Figure 8a clearly shows that in the absence of catalyst the UV–vis spectrum of the mixed solution remained unchanged for 25 min implying the extremely slow kinetics of the reduction of the ionized 4-nitrophenol (4-nitrophenolate) by $NaBH_4$. This is due to the repelling between the negatively charged 4-nitrophenolate and BH_4^- ions.[6] Figure 8b shows that the IrO_x catalyst has no activity toward the reduction of 4-nitrophenol by $NaBH_4$, as can be seen from unchanged UV–vis spectrum of the mixed solution after reaction for 25 min. Compared to the IrO_x NPs, the Ir catalyst exhibits obvious catalytic activity (Figure 8c). The absorption peak decreases to 45% of its original value after reaction for 25 min in the presence of Ir catalyst. It should be pointed out here that with

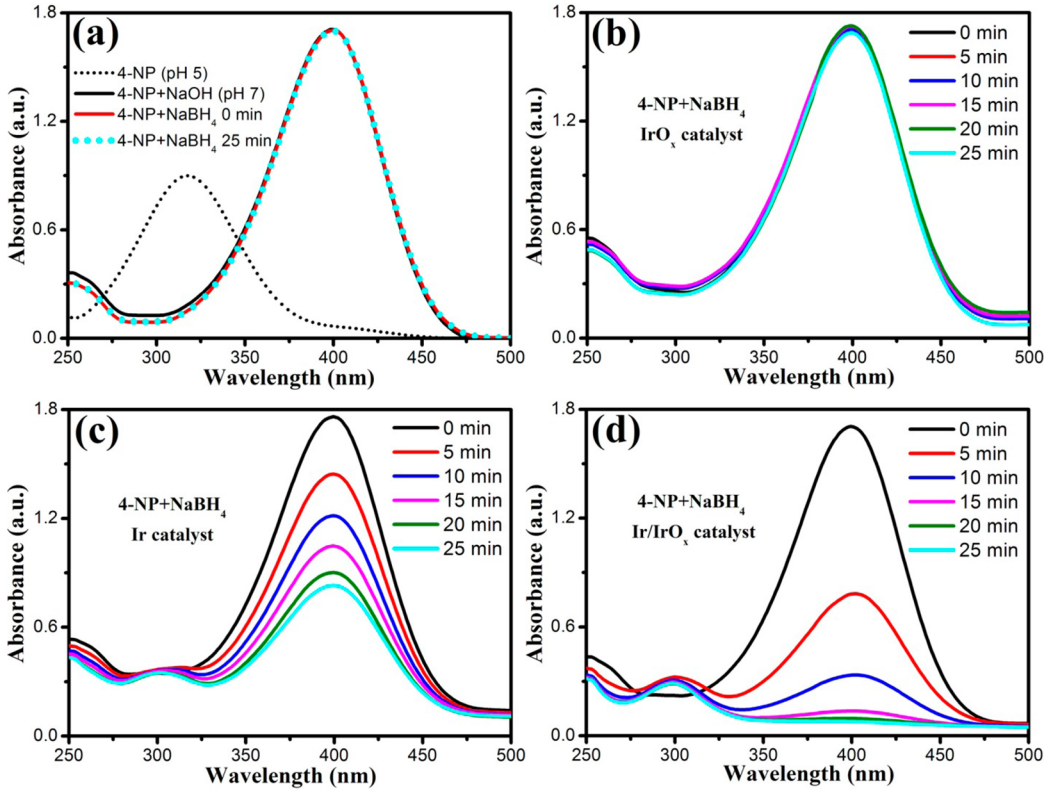

Figure 8. Time-dependent UV–vis spectra of a mixed aqueous solution of 50 μM 4-nitrophenol, 10 mM $NaBH_4$, and different catalysts: (a) no catalyst, (b) IrO_x, (c) Ir, and (d) Ir/IrO_x catalysts.

DOI: 10.1021/acsami.5b04504
ACS Appl. Mater. Interfaces 2015, 7, 16738–16749

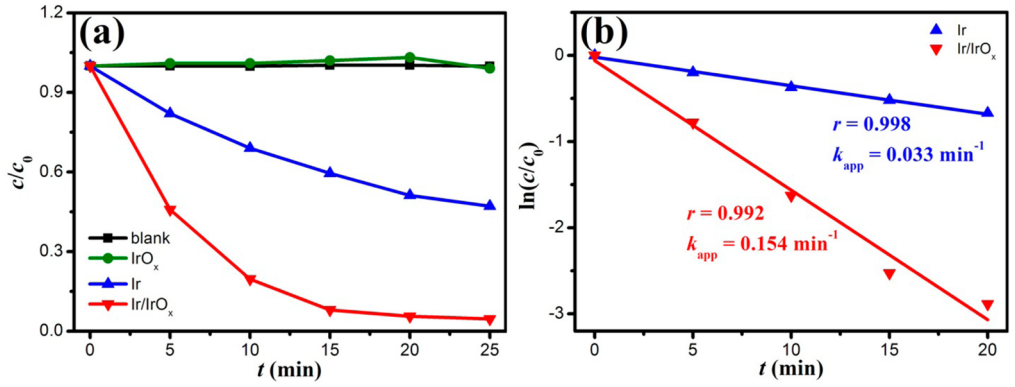

Figure 9. (a) Variation of c/c_0 versus reaction time for the reduction of 4-nitrophenol without any catalyst and with IrO_x, Ir, Ir/IrO_x as the catalyst. (b) Plot of $\ln(c/c_0)$ versus reaction time for the reduction of 4-nitrophenol with Ir or Ir/IrO_x as the catalyst. Here, c is the concentration of 4-nitrophenol at reaction time t, c_0 is the original concentration, and r is the correlation coefficient.

the decrease of the absorption peak at 400 nm a new peak appears at ca. 300 nm (Figure 8c). This absorption peak originates from the 4-aminophenol (Figure S3), which is the product of the reduction of 4-nitrophenol. Figure 8d demonstrates that among the three catalysts the Ir/IrO_x composite catalyst exhibits the highest catalytic activity for 4-nitrophenol reduction. When the Ir/IrO_x composite catalyst was added into the mixed solution, the absorption peak at 400 nm decreases to less than 50% of its initial value after reaction for only 5 min and completely disappears after reaction for 25 min. Moreover, we have ruled out the possibility that the decrease of UV−vis spectra is due to the adsorption of 4-nitrophenolate on the catalysts (Figure S4 in the Supporting Information). All these observations indicate fast kinetics for the reduction of 4-nitrophenol on the Ir/IrO_x composite catalyst.

The kinetics of the reduction of 4-nitrophenol in the presence of different catalysts was investigated, and the results are shown in Figure 9. According to the Beer−Lambert's Law, the absorbance is proportional to the concentration of the absorber.[58] Therefore, the value of c/c_0 is equal to that of A/A_0, where c_0 and A_0 are the original concentration and absorbance of 4-nitrophenolate, respectively, and c and A are the concentration and absorbance of 4-nitrophenolate at any time during the reaction, respectively. Figure 9a shows the variation of c/c_0 as a function of reaction time, which confirms that the catalytic activity decreases in the order Ir/IrO_x > Ir > IrO_x. Because an excessive amount of $NaBH_4$ was used in the reaction, the reduction of 4-nitrophenol follows the rules of a pseudo-first-order reaction.[59] Hence, the rate constant can be calculated via the following equations:

$$-\mathrm{d}c/\mathrm{d}t = k_{app}c \tag{5}$$

$$\ln(c/c_0) = -k_{app}t \tag{6}$$

where k_{app} is the apparent rate constant and t is the reaction time. Figure 9b shows the plots of $\ln(c/c_0)$ as a function of reaction time. The linear correlation between $\ln(c/c_0)$ and t for both the Ir and the Ir/IrO_x catalysts confirms that the reduction of 4-nitrophenol is a pseudo-first-order reaction.[59] The value of k_{app} for each catalyst can be obtained from the slope of the corresponding fitted line. For the Ir/IrO_x composite catalyst, k_{app} is 0.154 min^{-1}, which is nearly five times that (0.033 min^{-1}) for the Ir catalyst. To investigate whether the difference in catalytic activity originates from the difference in surface area of the catalysts, we measured the specific surface areas of the catalysts by using BET method. The specific surface areas of the Ir and the Ir/IrO_x catalysts were determined to be 272.457 and 71.560 m^2/g, respectively. Considering the amount of catalysts used in the reaction, the total surface areas (S) of the Ir and the Ir/IrO_x catalysts are 4.185×10^{-3} and 1.282×10^{-3} m^2, respectively. Therefore, the rate constant normalized to unit surface areas (k_n) can be obtained via the following equation according to the literature:[60]

$$k_n = k_{app}/S \tag{7}$$

where k_n can be used to describe the catalytic activity per unit surface area of the catalyst. Thus, k_n for Ir and Ir/IrO_x catalysts is calculated to be 7.93 and 120.15 m^{-2} min^{-1}, respectively. The activity per unit surface area of the Ir/IrO_x catalyst is over 15 times higher than that of Ir catalyst, providing strong evidence that the coexistence of Ir and IrO_x is crucial to the improvement of the catalytic activity of Ir.

The reduction of 4-nitrophenol by $NaBH_4$ follows eq 8 in an aqueous solution of pH 8.[6]

$$4O_2N\text{-}Ph\text{-}O^- + 3BH_4^- \rightarrow 4H_2N\text{-}Ph\text{-}O^- + 3BO_2^- + 2H_2O \tag{8}$$

where the Ph stands for a phenyl group. In the absence of catalyst, the high kinetic barrier between the mutually repelling BH_4^- and 4-nitrophenolate results in an extremely slow reaction rate, as is shown in Figure 8a. It has been reported that the transition metals such as Au,[45,61,62] Ag,[63,64] Pt−Ni,[46] Pd−Ag,[6] and Ni−Co[65] can catalyze the reduction of 4-nitrophenol by $NaBH_4$. It is widely accepted that the following two steps are involved in the transition-metal-catalyzed reduction of 4-nitrophenol by $NaBH_4$:[66,67] (1) The BH_4^- ions first chemically adsorb on metal surface and then release highly active hydrogen radicals, which are also adsorbed on metal surface. (2) The adsorbed hydrogen radicals react with adsorbed 4-nitrophenol (or 4-nitrophenolate) to produce 4-aminophenol (or 4-aminophenolate), or they react with water to generate H_2, which can reduce 4-nitrophenol (or 4-nitrophenolate) in solution. This is why the Ir catalyst exhibits catalytic activity toward the reduction of 4-nitrophenol (Figure 8c).

It has been demonstrated that treating the transition metal oxides with $NaBH_4$ can introduce an oxygen vacancy on the surface of the oxides.[68,69] Therefore, after the IrO_x was added

DOI: 10.1021/acsami.5b04504
ACS Appl. Mater. Interfaces 2015, 7, 16738−16749

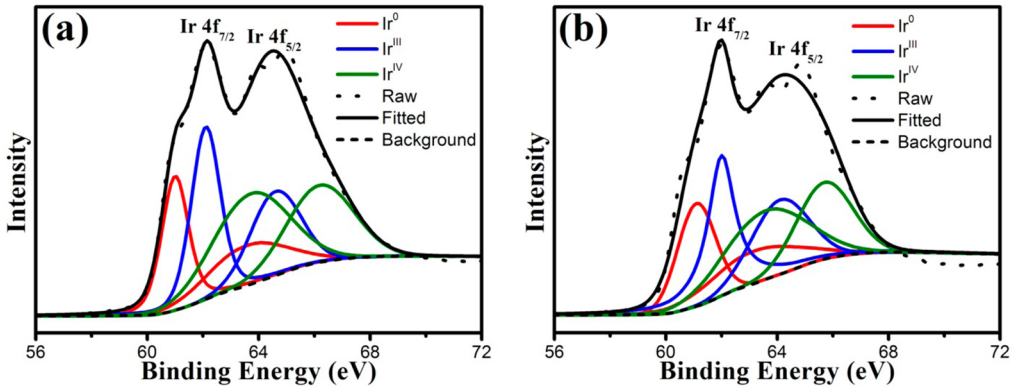

Figure 10. Ir 4f XPS spectra of Ir/IrO_x composite catalyst (a) before and (b) after being treated with 10 mM $NaBH_4$ at room temperature.

into the mixed solution of 4-nitrophenol and $NaBH_4$, oxygen vacancies were generated on its surface. Oxygen vacancies are positively charged, and they provide active sites for the adsorption of 4-nitrophenolate ions on the IrO_x surface. Although 4-nitrophenolate may adsorb on the surface of IrO_x, the IrO_x catalyst exhibits no activity toward 4-nitrophenol reduction (Figure 8b). This is because it is difficult for BH_4^- to adsorb on the IrO_x surface.

As for the Ir/IrO_x composite catalyst, the combination of Ir and IrO_x provides large amount of Ir/IrO_x interfaces, which are the active sites for the reduction of 4-nitrophenol by $NaBH_4$. On one hand, the BH_4^- ions are adsorbed on the Ir side of the Ir/IrO_x interfaces and generate highly active hydrogen radicals that are stabilized on Ir surface. On the other hand, the oxygen vacancies, which were generated on the surface of IrO_x by $NaBH_4$, provided active sites for the adsorption of 4-nitrophenolate. XPS was employed to quantitatively characterize the degree of oxygen vacancy produced in the Ir/IrO_x composite catalysts. Figure 10 shows the Ir 4f spectra of the composite catalysts before and after being treated with $NaBH_4$ at room temperature. According to previous work,[70] both of the spectra can be deconvoluted into three pairs of peaks, which correspond to the binding energies of metallic Ir (Ir^0), Ir^{3+}, and Ir^{4+}, respectively. On the basis of the variation in the percentages of Ir^{4+} and Ir^{3+} before and after treated with $NaBH_4$, the degree of oxygen vacancy is estimated to be ca. 2.5%. The details of the estimation are presented in the Supporting Information.

The Ir/IrO_x interface provides both the metal surface on the Ir side and the oxygen vacancy on the IrO_x side, which ensures the adsorption of BH_4^- and 4-nitrophenolate, respectively. As a result, 4-nitrophenolate has more chances to be reduced at the Ir/IrO_x interface rather than in solution. Moreover, after the reaction, the electron-withdrawing nitro group is reduced to an electron-donating amino group, which results in an increase of the proton affinity of the substituted phenolate. Therefore, the produced 4-aminophenolate ions are much easier to combine with protons and then desorb from the oxygen vacancy, leaving the active sites open again for 4-nitrophenolate adsorption. Therefore, the synergic effect of the Ir and IrO_x at the Ir/IrO_x interface greatly enhances the reaction rate, which is why the Ir/IrOx composite catalyst exhibits even higher catalytic activity than that of the Ir catalyst.

Stability is a critical issue for the long-term application of catalysts. To examine the stability of the Ir/IrO_x catalyst, consecutive reaction cycles were carried out in the presence of Ir/IrO_x catalyst. After reaction for 40 min, the absorption peak at 400 nm disappears (Figure S5a–e in the Supporting Information), indicating the completion of the reaction. Then, 4-nitrophenol and fresh $NaBH_4$ were injected into the reaction system to trigger the next run of the reaction. In each reaction run, 4-nitrophenol can be completely reduced to 4-aminophenol, indicating that the catalytic activity of Ir/IrO_x is conserved after successive reaction cycles (Figure S5a–e). Because all the experiment runs were conducted in the same reaction cell, the accumulation of 4-aminophenol with increasing reaction cycle was observed (Figure S5f). Figure 11 shows the decrease of the concentration of 4-nitrophenol as

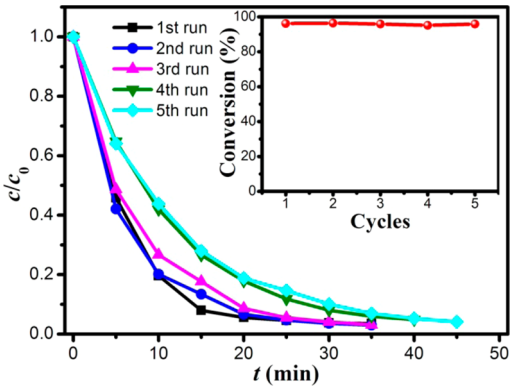

Figure 11. Variation of c/c_0 versus reaction time for the reduction of 4-nitrophenol in the presence of Ir/IrO_x catalyst during five consecutive runs. Inset is the conversion efficiency of each reaction run.

a function of reaction time in each reaction run. The final conversion efficiency of 4-nitrophenol is around 96% and almost remains constant after repeated reaction runs (inset of Figure 11), indicating high stability of the composite catalyst. Another important parameter to assess stability of metal-based catalysts is the leaching of the active phase to the reaction medium. To determine the leaching of the catalyst during the consecutive reaction cycles, the catalyst was separated from the reaction solution after the fifth cycle, and the solution was subjected to inductively coupled plasma-atomic emission spectroscopy to quantify the concentration of Ir ions leached into the solution. The result indicates an Ir loss of ca. 0.3% after 5 cycles, providing solid evidence that the Ir/IrO_x catalyst is highly stable during repeated reaction runs.

DOI: 10.1021/acsami.5b04504
ACS Appl. Mater. Interfaces 2015, 7, 16738–16749

4. CONCLUSIONS

The IrO_x NPs with diameter of 1.7 ± 0.3 nm have been successfully produced via a facile one-step photochemical route. UV−vis irradiation initiates the hydrolysis of iridium precursor and the generation of IrO_x NPs, and there exists a threshold wavelength of 500 nm for the photochemical reaction. Only when the incident wavelength is shorter than 500 nm can the photochemical reaction occur. The generation rate of IrO_x NPs can be modulated by tuning the incident wavelength: the shorter the wavelength, the faster the reaction rate. The Ir/IrO_x composite has been fabricated by partial reduction of IrO_x NPs with $NaBH_4$ at 90 °C. The Ir/IrO_x composite catalyst exhibits good catalytic activity and high stability toward the reduction of 4-nitrophenol.

■ ASSOCIATED CONTENT

Supporting Information

UV−vis spectra of freshly prepared and aged IrO_x nanoparticle colloid solution and aqueous solution of 4-aminophenol; time-dependent UV−vis spectra of basic $IrCl_3$ solution under 2 h UV irradiation followed by 2 h in the dark and under 1 h UV irradiation followed by 3 h in the dark, 4-nitrophenol with different catalysts, and mixed solution of 4-nitrophenol, $NaBH_4$, and Ir/IrO_x catalyst in five consecutive experimental cycles; details of estimation of the degree of oxygen vacancy on the basis of the XPS data. The Supporting Information is available free of charge on the ACS Publications website at DOI: 10.1021/acsami.5b04504.

■ AUTHOR INFORMATION

Corresponding Author

*Tel.: +86 01 82339562. Fax: +86 01 82339562. E-mail: pdiao@buaa.edu.cn.

Notes

The authors declare no competing financial interest.

■ ACKNOWLEDGMENTS

We gratefully acknowledge the financial support of this work by the National Natural Science Foundation of China (NSFC 21173016), Beijing Natural Science Foundation (2142020 and 2151001).

■ ABBREVIATIONS

NPs, nanoparticles; UV−vis, ultraviolet−visible; TEM, transmission electron microscopy; XRD, X-ray diffraction; BET, Brunauer−Emmett−Teller; XPS, X-ray photoelectron spectroscopy

■ REFERENCES

(1) Wang, J. Y.; Diao, P.; Zhang, Q. Dual Detection Strategy for Electrochemical Analysis of Glucose and Nitrite Using a Partitionally Modified Electrode. *Analyst* **2012**, *137*, 145−152.
(2) Li, Y. Y.; Diao, P.; Jin, T.; Sun, J.; Xu, D. Shape-Controlled Electrodeposition of Standing Rh Nanoplates on Indium Tin Oxide Substrates and Their Electrocatalytic Activity toward Formic Acid Oxidation. *Electrochim. Acta* **2012**, *83*, 146−154.
(3) Nakagawa, T.; Bjorge, N. S.; Murray, R. W. Electrogenerated IrO_x Nanoparticles as Dissolved Redox Catalysts for Water Oxidation. *J. Am. Chem. Soc.* **2009**, *131*, 15578−15579.
(4) Zhang, D. F.; Diao, P. Activity and Stability of Supported Gold Nano- and Submicro-Particles toward the Electrocatalytic Oxidation of Carbon Monoxide. *Appl. Catal., A* **2014**, *469*, 65−73.
(5) Tian, N.; Zhou, Z. Y.; Sun, S. G.; Ding, Y.; Wang, Z. L. Synthesis of Tetrahexahedral Platinum Nanocrystals with High-Index Facets and High Electro-Oxidation Activity. *Science* **2007**, *316*, 732−735.
(6) Huang, J. F.; Vongehr, S.; Tang, S. C.; Lu, H. M.; Meng, X. K. Highly Catalytic Pd-Ag Bimetallic Dendrites. *J. Phys. Chem. C* **2010**, *114*, 15005−15010.
(7) Wang, Y. L.; Camargo, P. H. C.; Skrabalak, S. E.; Gu, H. C.; Xia, Y. N. A Facile, Water-Based Synthesis of Highly Branched Nanostructures of Silver. *Langmuir* **2008**, *24*, 12042−12046.
(8) Zhang, D. F.; Diao, P.; Zhang, Q. Potential-Induced Shape Evolution of Gold Nanoparticles Prepared on ITO Substrate. *J. Phys. Chem. C* **2009**, *113*, 15796−15800.
(9) Xu, D.; Yan, X. H.; Diao, P.; Yin, P. G. Electrodeposition of Vertically Aligned Palladium Nanoneedles and Their Application as Active Substrates for Surface-Enhanced Raman Scattering. *J. Phys. Chem. C* **2014**, *118*, 9758−9768.
(10) He, Y. B.; Li, G. R.; Wang, Z. L.; Ou, Y. N.; Tong, Y. X. Pt Nanorods Aggregates with Enhanced Electrocatalytic Activity toward Methanol Oxidation. *J. Phys. Chem. C* **2010**, *114*, 19175−19181.
(11) Gacem, N.; Diao, P. Effect of Solvent Polarity on the Assembly Behavior of PVP Coated Rhodium Nanoparticles. *Colloids Surf., A* **2013**, *417*, 32−38.
(12) Baida, H.; Diao, P. Preparation of Iridium Nano- and Submicroparticles on Solid Substrates by Direct Surface Growth and Drop-Drying Assembly. *Rare Met.* **2012**, *31*, 523−530.
(13) Zhao, C. X.; Yu, H. T.; Li, Y. C.; Li, X. H.; Ding, N.; Fan, L. Z. Electrochemical Controlled Synthesis and Characterization of Well-Aligned IrO_2 Nanotube Arrays with Enhanced Electrocatalytic Activity toward Oxygen Evolution Reaction. *J. Electroanal. Chem.* **2013**, *688*, 269−274.
(14) Xue, C.; Métraux, G. S.; Millstone, J. E.; Mirkin, C. A. Mechanistic Study of Photomediated Triangular Silver Nanoprism Growth. *J. Am. Chem. Soc.* **2008**, *130*, 8337−8344.
(15) Nakajima, T.; Shinoda, K.; Tsuchiya, T. UV-Assisted Nucleation and Growth of Oxide Films From Chemical Solutions. *Chem. Soc. Rev.* **2014**, *43*, 2027−2041.
(16) Sakamoto, M.; Majima, T. Photochemistry for the Synthesis of Noble Metal Nanoparticles. *Bull. Chem. Soc. Jpn.* **2010**, *83*, 1133−1154.
(17) Zhang, J.; Langille, M. R.; Mirkin, C. A. Synthesis of Silver Nanorods by Low Energy Excitation of Spherical Plasmonic Seeds. *Nano Lett.* **2011**, *11*, 2495−2498.
(18) Wu, X. M.; Redmond, P. L.; Liu, H. T.; Chen, Y. H.; Steigerwald, M.; Brus, L. Photovoltage Mechanism for Room Light Conversion of Citrate Stabilized Silver Nanocrystal Seeds to Large Nanoprisms. *J. Am. Chem. Soc.* **2008**, *130*, 9500−9506.
(19) Tanabe, I.; Matsubara, K.; Sakai, N.; Tatsuma, T. Photoelectrochemical and Optical Behavior of Single Upright Ag Nanoplates on a TiO_2 Film. *J. Phys. Chem. C* **2011**, *115*, 1695−1701.
(20) Jin, R. C.; Cao, Y. W.; Mirkin, C. A.; Kelly, K. L.; Schatz, G. C.; Zheng, J. G. Photoinduced Conversion of Silver Nanospheres to Nanoprisms. *Science* **2001**, *294*, 1901−1903.
(21) Huang, Y. J.; Kim, D. H. Light-Controlled Synthesis of Gold Nanoparticles Using a Rigid, Photoresponsive Surfactant. *Nanoscale* **2012**, *4*, 6312−6317.
(22) Kundu, S.; Wang, K.; Lau, S.; Liang, H. Photochemical Synthesis of Shape-Selective Palladium Nanocubes in Aqueous Solution. *J. Nanopart. Res.* **2010**, *12*, 2799−2811.
(23) Kundu, S.; Liang, H. Photoinduced Formation of Shape-Selective Pt Nanoparticles. *Langmuir* **2010**, *26*, 6720−6727.
(24) Kundu, S.; Liang, H. Shape-Selective Formation and Characterization of Catalytically Active Iridium Nanoparticles. *J. Colloid Interface Sci.* **2011**, *354*, 597−606.
(25) Smith, R. D. L.; Sporinova, B.; Fagan, R. D.; Trudel, S.; Berlinguette, C. P. Facile Photochemical Preparation of Amorphous Iridium Oxide Films for Water Oxidation Catalysis. *Chem. Mater.* **2014**, *26*, 1654−1659.
(26) Zhao, Y. X.; Hernandez-Pagan, E. A.; Vargas-Barbosa, N. M.; Dysart, J. L.; Mallouk, T. E. A High Yield Synthesis of Ligand-Free

DOI: 10.1021/acsami.5b04504
ACS Appl. Mater. Interfaces 2015, 7, 16738−16749

Iridium Oxide Nanoparticles with High Electrocatalytic Activity. *J. Phys. Chem. Lett.* **2011**, *2*, 402−406.
(27) Ioroi, T.; Kitazawa, N.; Yasuda, K.; Yamamoto, Y.; Takenaka, H. Iridium Oxide/Platinum Electrocatalysts for Unitized Regenerative Polymer Electrolyte Fuel Cells. *J. Electrochem. Soc.* **2000**, *147*, 2018−2022.
(28) Diao, P.; Zhang, D. F.; Wang, J. Y.; Zhang, Q. Electrocatalytic Activity of Supported Gold Nanoparticles toward CO Oxidation: The Perimeter Effect of Gold−Support Interface. *Electrochem. Commun.* **2010**, *12*, 1622−1625.
(29) Diao, P.; Zhang, D.; Guo, M.; Zhang, Q. Electrocatalytic Oxidation of CO on Supported Gold Nanoparticles and Submicroparticles: Support and Size Effects in Electrochemical Systems. *J. Catal.* **2007**, *250*, 247−253.
(30) Comotti, M.; Li, W. C.; Spliethoff, B.; Schüth, F. Support Effect in High Activity Gold Catalysts for CO Oxidation. *J. Am. Chem. Soc.* **2006**, *128*, 917−924.
(31) Zhang, H. J.; Li, X. Y.; Chen, G. H. Ionic liquid-Facilitated Synthesis and Catalytic Activity of Highly Dispersed Ag Nanoclusters Supported on TiO_2. *J. Mater. Chem.* **2009**, *19*, 8223−8231.
(32) Liu, Y. P.; Chung, J.; Jang, Y.; Mao, S.; Kim, B. M.; Wang, Y. Q.; Guo, X. H. Magnetically Recoverable Nanoflake-Shaped Iron Oxide/Pt Heterogeneous Catalysts and Their Excellent Catalytic Performance in the Hydrogenation Reaction. *ACS Appl. Mater. Interfaces* **2014**, *6*, 1887−1892.
(33) Dhokale, R. K.; Yadav, H. M.; Achary, S. N.; Delekar, S. D. Anatase Supported Nickel Nanoparticles for Catalytic Hydrogenation of 4-Nitrophenol. *Appl. Surf. Sci.* **2014**, *303*, 168−174.
(34) Li, Y. H.; Zhang, Q.; Zhang, N. W.; Zhu, L. H.; Zheng, J. B.; Chen, B. H. Ru−RuO_2/C as an Efficient Catalyst for the Sodium Borohydride Hydrolysis to Hydrogen. *Int. J. Hydrogen Energy* **2013**, *38*, 13360−13367.
(35) Kinnunen, N. M.; Hirvi, J. T.; Suvanto, M.; Pakkanen, T. A. Role of the Interface between Pd and PdO in Methane Dissociation. *J. Phys. Chem. C* **2011**, *115*, 19197−19202.
(36) He, X.; Yang, H. M. Au Nanoparticles Assembled on Palygorskite: Enhanced Catalytic Property and Au−Au_2O_3 Coexistence. *J. Mol. Catal. A: Chem.* **2013**, *379*, 219−224.
(37) Liu, Y. J.; Wang, D. G.; Sun, B.; Zhu, X. M. Aqueous 4-Nitrophenol Decomposition and Hydrogen Peroxide Formation Induced by Contact Glow Discharge Electrolysis. *J. Hazard. Mater.* **2010**, *181*, 1010−1015.
(38) Corbett, J. F. An Historical Review of the Use of Dye Precursors in the Formulation of Commercial Oxidation Hair Dyes. *Dyes Pigm.* **1999**, *41*, 127−136.
(39) Lunar, L.; Sicilia, D.; Rubio, S.; Pérez-Bendito, D.; Nickel, U. Degradation of Photographic Developers by Fenton's Reagent: Condition Optimization and Kinetics for Metol Oxidation. *Water Res.* **2000**, *34*, 1791−1802.
(40) Chang, Y. C.; Chen, D. H. Catalytic Reduction of 4-Nitrophenol by Magnetically Recoverable Au Nanocatalyst. *J. Hazard. Mater.* **2009**, *165*, 664−669.
(41) Razo-Flores, E.; Donlon, B.; Lettinga, G.; Field, J. A. Biotransformation and Biodegradation of N-Substituted Aromatics in Methanogenic Granular Sludge. *FEMS Microbiol. Rev.* **1997**, *20*, 525−538.
(42) Afzal Khan, S.; Hamayun, M.; Ahmed, S. Degradation of 4-Aminophenol by Newly Isolated Pseudomonas sp. strain ST-4. *Enzyme Microb. Technol.* **2006**, *38*, 10−13.
(43) Du, Y.; Chen, H. L.; Chen, R. Z.; Xu, N. P. Synthesis of p-Aminophenol from p-Nitrophenol over Nano-Sized Nickel Catalysts. *Appl. Catal., A* **2004**, *277*, 259−264.
(44) Zhang, Z. Y.; Shao, C. L.; Sun, Y. Y.; Mu, J. B.; Zhang, M. Y.; Zhang, P.; Guo, Z. C.; Liang, P. P.; Wang, C. H.; Liu, Y. C. Tubular Nanocomposite Catalysts Based on Size-Controlled and Highly Dispersed Silver Nanoparticles Assembled on Electrospun Silica Nanotubes for Catalytic Reduction of 4-Nitrophenol. *J. Mater. Chem.* **2012**, *22*, 1387−1395.
(45) Zeng, J.; Zhang, Q.; Chen, J.; Xia, Y. A Comparison Study of the Catalytic Properties of Au-Based Nanocages, Nanoboxes, and Nanoparticles. *Nano Lett.* **2010**, *10*, 30−35.
(46) Ghosh, S. Bimetallic Pt-Ni Nanoparticles Can Catalyze Reduction of Aromatic Nitro Compounds by Sodium Borohydride in Aqueous Solution. *Appl. Catal., A* **2004**, *268*, 61−66.
(47) Tonbul, Y.; Zahmakiran, M.; Özkar, S. Iridium(0) Nanoparticles Dispersed in Zeolite Framework: A Highly Active and Long-Lived Green Nanocatalyst for the Hydrogenation of Neat Aromatics at Room Temperature. *Appl. Catal., B* **2014**, *148−149*, 466−472.
(48) Peera, S. G.; Sahu, A. K.; Bhat, S. D.; Lee, S. C. Nitrogen Functionalized Graphite Nanofibers/Ir Nanoparticles for Enhanced Oxygen Reduction Reaction in Polymer Electrolyte Fuel Cells (PEFCs). *RSC Adv.* **2014**, *4*, 11080−11088.
(49) Chang, J. C.; Garner, C. S. Kinetics of Aquation of Aquopentachloroiridate (III) and Chloride Anation of Diaquotetrachloroiridate (III) Anions. *Inorg. Chem.* **1965**, *4*, 209−215.
(50) Poulsen, I. A.; Garner, C. S. A Thermodynamic and Kinetic Study of Hexachloro and Aquopentachloro Complexes of Iridium(III) in Aqueous Solutions. *J. Am. Chem. Soc.* **1962**, *84*, 2032−2037.
(51) Chen, J. Y.; Chen, Y. M.; Sun, Y.; Lee, J. F.; Chen, S. Y.; Chen, P. C.; Wu, P. W. Chemical Bath Deposition of IrO_2 Films on ITO Substrate. *Ceram. Int.* **2014**, *40*, 14983−14990.
(52) Nakagawa, T.; Beasley, C. A.; Murray, R. W. Efficient Electro-Oxidation of Water near Its Reversible Potential by a Mesoporous IrO_x Nanoparticle Film. *J. Phys. Chem. C* **2009**, *113*, 12958−12961.
(53) Nahor, C. S.; Hapiot, P.; Neta, P.; Harriman, A. Changes in the Redox State of Iridium Oxide Clusters and Their Relation to Catalytic Water Oxidation. Radiolytic and Electrochemical Studies. *J. Phys. Chem.* **1991**, *95*, 616−621.
(54) Niesz, K.; Reji, C.; Neilson, J. R.; Vargas, R. C.; Morse, D. E. Unusual Evolution of Ceria Nanocrystal Morphologies Promoted by a Low-Temperature Vapor Diffusion Based Process. *Cryst. Growth Des.* **2010**, *10*, 4485−4490.
(55) Chen, W.; Chen, S. W. Iridium-Platinum Alloy Nanoparticles: Composition-Dependent Electrocatalytic Activity for Formic Acid Oxidation. *J. Mater. Chem.* **2011**, *21*, 9169−9178.
(56) Sivakumar, S.; Anusuya, D.; Khatiwada, C. P.; Sivasubramanian, J.; Venkatesan, A.; Soundhirarajan, P. Characterizations of Diverse Mole of Pure and Ni-Doped α-Fe_2O_3 Synthesized Nanoparticles Through Chemical Precipitation Route. *Spectrochim. Acta, Part A* **2014**, *128*, 69−75.
(57) Praharaj, S.; Nath, S.; Ghosh, S. K.; Kundu, S.; Pal, T. Immobilization and Recovery of Au Nanoparticles from Anion Exchange Resin: Resin-Bound Nanoparticle Matrix as a Catalyst for the Reduction of 4-Nitrophenol. *Langmuir* **2004**, *20*, 9889−9892.
(58) Koenig, J. F.; Martel, D. Applying UV-Vis Spectroscopy to Step-by-Step Molecular Self Assembly on Surface: Does it Bring Pertinent Information? *Thin Solid Films* **2008**, *516*, 3865−3872.
(59) Wunder, S.; Polzer, F.; Lu, Y.; Mei, Y.; Ballauff, M. Kinetic Analysis of Catalytic Reduction of 4-Nitrophenol by Metallic Nanoparticles Immobilized in Spherical Polyelectrolyte Brushes. *J. Phys. Chem. C* **2010**, *114*, 8814−8820.
(60) Panigrahi, S.; Basu, S.; Praharaj, S.; Pande, S.; Jana, S.; Pal, A.; Ghosh, S. K.; Pal, T. Synthesis and Size-Selective Catalysis by Supported Gold Nanoparticles: Study on Heterogeneous and Homogeneous Catalytic Process. *J. Phys. Chem. C* **2007**, *111*, 4596−4605.
(61) Esumi, K.; Miyamoto, K.; Yoshimura, T. Comparison of PAMAM-Au and PPI-Au Nanocomposites and Their Catalytic Activity for Reduction of 4-Nitrophenol. *J. Colloid Interface Sci.* **2002**, *254*, 402−405.
(62) Corma, A.; Concepción, P.; Serna, P. A Different Reaction Pathway for the Reduction of Aromatic Nitro Compounds on Gold Catalysts. *Angew. Chem., Int. Ed.* **2007**, *46*, 7266−7269.
(63) Saha, S.; Pal, A.; Kundu, S.; Basu, S.; Pal, T. Photochemical Green Synthesis of Calcium-Alginate-Stabilized Ag and Au Nanoparticles and Their Catalytic Application to 4-Nitrophenol Reduction. *Langmuir* **2010**, *26*, 2885−2893.

DOI: 10.1021/acsami.5b04504
ACS Appl. Mater. Interfaces 2015, 7, 16738−16749

(64) Pradhan, N.; Pal, A.; Pal, T. Silver Nanoparticle Catalyzed Reduction of Aromatic Nitro Compounds. *Colloids Surf., A* **2002**, *196*, 247−257.
(65) Wu, K. L.; Wei, X. W.; Zhou, X. M.; Wu, D. H.; Liu, X. W.; Ye, Y.; Wang, Q. $NiCo_2$ Alloys: Controllable Synthesis, Magnetic Properties, and Catalytic Applications in Reduction of 4-Nitrophenol. *J. Phys. Chem. C* **2011**, *115*, 16268−16274.
(66) Escaño, M. C. S.; Gyenge, E.; Arevalo, R. L.; Kasai, H. Reactivity Descriptors for Borohydride Interaction with Metal Surfaces. *J. Phys. Chem. C* **2011**, *115*, 19883−19889.
(67) Kumar Barman, B.; Kar Nanda, K. Uninterrupted Galvanic Reaction for Scalable and Rapid Synthesis of Metallic and Bimetallic Sponges/Dendrites as Efficient Catalysts for 4-Nitrophenol Reduction. *Dalton Trans.* **2015**, *44*, 4215−4222.
(68) Kang, Q.; Cao, J. Y.; Zhang, Y. J.; Liu, L. Q.; Xu, H.; Ye, J. H. Reduced TiO_2 Nanotube Arrays for Photoelectrochemical Water Splitting. *J. Mater. Chem. A* **2013**, *1*, 5766−5774.
(69) Wang, C.; Wu, D.; Wang, P.; Ao, Y.; Hou, J.; Qian, J. Effect of Oxygen Vacancy on Enhanced Photocatalytic Activity of Reduced ZnO Nanorod Arrays. *Appl. Surf. Sci.* **2015**, *325*, 112−116.
(70) Allagui, A.; Oudah, M.; Tuaev, X.; Ntais, S.; Almomani, F.; Baranova, E. A. Ammonia Electro-Oxidation on Alloyed PtIr Nanoparticles of Well-Defined Size. *Int. J. Hydrogen Energy* **2013**, *38*, 2455−2463.

DOI: 10.1021/acsami.5b04504
ACS Appl. Mater. Interfaces 2015, 7, 16738−16749